Journal of Biomechanics 152 (2023) 111591

Contents lists available at ScienceDirect

Journal of Biomechanics

journal homepage: www.elsevier.com/locate/jbiomech

Instabilities induced by mechanical loading determine the viability of chondrocytes grown on porous scaffolds

Byumsu Kim [a], Nikolaos Bouklas [a], Itai Cohen [b], Lawrence J. Bonassar [a,c,*]

[a] Sibley School of Mechanical and Aerospace Engineering, Cornell University, Ithaca, NY, United States
[b] Department of Physics, Cornell University, Ithaca, NY, United States
[c] Meinig School of Biomedical Engineering, Cornell University, Ithaca, NY, United States

ARTICLE INFO

Keywords:
Soft Porous Materials
Instabilities
Tissue Engineering
Digital Image Correlation
Chondrocyte Mechanobiology

ABSTRACT

Tissue-engineered cartilage constructs have shown promise to treat focal cartilage defects in multiple clinical studies. Notably, products in clinical use or in late-stage clinical trials often utilize porous collagen scaffolds to provide mechanical support and attachment sites for chondrocytes. Under loading, both the local mechanical responses of collagen scaffolds and the corresponding cellular outcomes are poorly understood, despite their wide use. As such, the architecture of collagen scaffolds varies significantly among tissue-engineered cartilage products, but the effects of such architectures on construct mechanics and cell viability are not well understood. This study investigated the effects of local mechanical responses of collagen scaffolds on chondrocyte viability in tissue-engineered cartilage constructs. We utilized fast confocal microscopy combined with a strain mapping technique to analyze the architecture-dependent instabilities under quasi-static loading and subsequent chondrocyte death in honeycomb and sponge scaffolds. More specifically, we compared the isotropic and the orthotropic planes for each type of collagen scaffold. Under compression, both planes exhibited elastic, buckled, and densified deformation modes. In both loading directions, cell death was minimal in regions that experienced elastic deformation mode and a trend of increase in buckled mode. More interestingly, we saw a significant increase in cell death in densified mode. Overall, this study suggests that local instabilities are directly correlated to chondrocyte death in tissue-engineered cartilage constructs, highlighting the importance of understanding the architecture-dependent local mechanical responses under loading.

1. Introduction

Cartilage serves a purely mechanical function, providing lubrication and load transmission for joints. Despite its critical mechanical role, cartilage has a limited healing capacity when damaged. Therefore, tissue engineering techniques have been investigated extensively over the last two decades to address the innate lack of regenerative properties of cartilage. Such techniques have shown promising results for healing and regenerating damaged cartilage tissue (Anderson et al., 2017; Crawford et al., 2012; Kreuz et al., 2011; Ossendorf et al., 2007; Schneider et al., 2011). In fact, multiple tissue-engineered products are commercially available or are undergoing clinical trials (Jiang et al., 2020).

Cartilage tissue engineering techniques often utilize scaffolds to provide structure for cell attachment and proliferation (Murphy et al., 2010; Murphy and O'Brien, 2010) as well as initial mechanical support. Several scaffold materials, such as poly-lactic-acid (Moran et al., 2003), hydrogels (Lee et al., 2007; Rouillard et al., 2011), and hydroxyapatite (Vansusante et al., 1998), have been investigated as vehicles to carry chondrocytes and stem cells in preclinical studies. Notably, porous collagen scaffolds have emerged as an effective vehicle for transplanting chondrocytes for clinical applications. Such constructs can be implanted immediately after seeding (MACI®, NOVOCART® 3D) (Brittberg et al., 2018; Zak et al., 2014) or cultured extensively prior to implantation (NeoCart®), which dramatically changes the mechanical properties of the constructs (Crawford et al., 2012; Middendorf et al., 2020a, 2020b).

At the early stage of the tissue manufacturing process, scaffold mechanical properties dictate the responses of the tissue-engineered constructs. Multiple studies in cellular solids and porous materials have been extended to understand the mechanics of collagen scaffolds (Gibson, 2005; Harley et al., 2007). The mechanics of soft foams /

* Corresponding author at: Daljit S. and Elaine Sarkaria Professor, Meinig School of Biomedical Engineering, Sibley School of Mechanical and Aerospace Engineering, 149 Weill Hall, Cornell University, Ithaca, NY 14853, United States.
E-mail address: lb244@cornell.edu (L.J. Bonassar).

https://doi.org/10.1016/j.jbiomech.2023.111591
Accepted 11 April 2023
Available online 13 April 2023

sponges are complicated and display non-linear behavior due to the combination of the complexity of the scaffold architecture combined with poro-viscoelastic properties of collagen (Silver et al., 2002; Wang et al., 1997). More specifically, collagen scaffolds have been shown to exhibit non-linear yet reversible instabilities under compression, leading to complex strain distributions (Kim et al., 2022).

Numerous studies have demonstrated that chondrocyte behaviors such as cell death (Bartell et al., 2015; Bonnevie et al., 2018), apoptosis (Delco et al., 2018), and cell signaling (Madden et al., 2015), are related to the micromechanical environment of native cartilage explants. In particular, the relationship between macroscale applied loading and local strain including cellular deformation is crucial (Guilak et al., 1995). Furthermore, previous studies have demonstrated that chondrocyte behavior in engineered constructs may be different compared to the native tissue, most likely due to differences in local environment (Genes et al., 2004; Lee et al., 2017). However, the relationship between micromechanical environment and chondrocyte behavior in tissue-engineered constructs is understudied, and yet critical for determining the viability of these constructs. Understanding this relationship is critical to optimize tissue-engineered constructs to minimize adverse cellular responses.

Previous investigations in cartilage micromechanical environment were primarily focused on native tissue and chondrocytes in agarose gels (Buschmann et al., 1995, 1992; Guilak, 2000; Guilak et al., 1995, 1994). Notably, the local mechanics of porous scaffolds is distinct from gels. For example, within porous scaffolds, instabilities can lead to large zones of strain localization which significantly alters the micromechanical environment of the chondrocytes. Such strain localization is absent in both hydrogels and native tissue. The effect of such high levels of strain localization is unclear, and the relationship between chondrocyte viability and the unique micromechanical environment of tissue-engineered constructs made using porous scaffold is poorly understood.

As such, the objective of this study was to investigate the relationship between the micromechanical environment generated by local instabilities, the architecture of collagen scaffolds, and the resulting chondrocyte behavior in tissue-engineered cartilage constructs under loading. We manufactured the constructs with honeycomb and sponge architectures using commercially available type 1 collagen made from a freeze-drying process. We (i) compared the strain distribution in two different loading directions, (ii) identified local regions of the constructs experiencing elastic, buckling, and densification deformation modes, and (iii) compared the cell viability of chondrocytes in regions experiencing elastic, buckling, and densification deformation modes.

2. Materials and methods

2.1. Tissue-Engineered cartilage construct preparation

Femoral condyles were sterilely harvested from the articular joints of neonatal bovids (Gold Medal Packing, Oriskany, NY). Chondrocytes were isolated by digesting the condyles with 0.3 % w/v collagenase type II (Cappel Worthington Biochemicals, Malvern, PA) for 12 to 18 h. Isolated chondrocytes were mixed with 3 mg/ml rat tail collagen (Bowles et al., 2010; Cross et al., 2010) at a concentration of 10×10^6 cells/ml. The mixture was then seeded onto 6 mm diameter by 1.5 mm height type I collagen honeycomb (Histogenics Corp., Waltham, MA) and sponge scaffolds (Koken CO., LTD, Tokyo, Japan). A total of 14 tissue-engineered constructs (6 with honeycomb scaffolds and 8 with sponge scaffolds) were cultured in Dulbecco's Modified Eagle's Medium (VWR International, Radnor, PA) supplemented with 10% fetal bovine serum (GeminiBio, West Sacramento, CA) and 1% antibiotic and antimycotic for 48 h under low oxygen (<5%) conditions at 37 °C and 5% CO_2 in

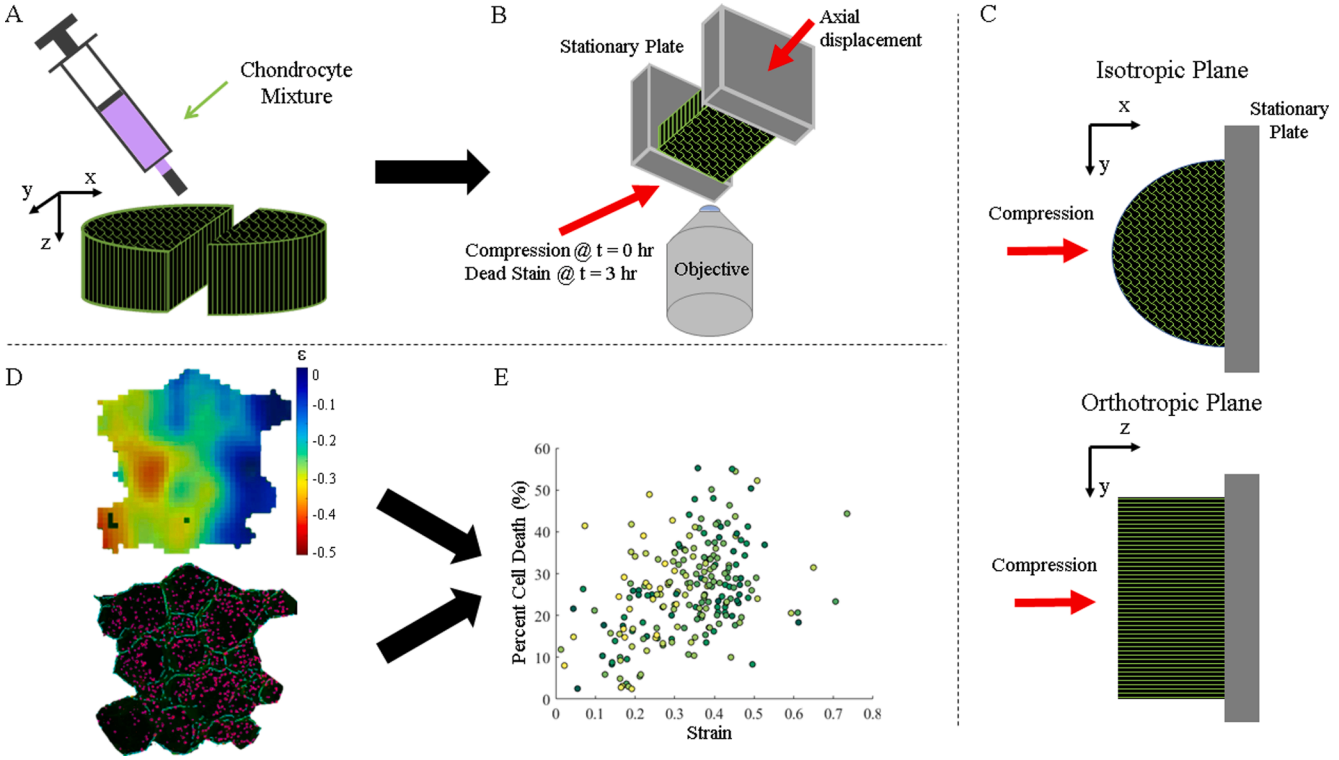

Fig. 1. Analysis methods for tissue-engineered cartilage construct. A. Chondrocytes were mixed with collagen and seeded in honeycomb and sponge collagen scaffolds. The constructs were cultured for 48 h. B. Tissue-engineered constructs were loaded in Tissue Deformation Imaging Stage and axially compressed. Compressive mechanical behavior of the constructs was recorded. Ethidium homodimer – 1 was added after compression to detect dead cells due to the compression. C. Compression was applied to both isotropic and orthotropic planes. D. From the compression video, local strain was analyzed. From the EthD-1 stain image, the number and location of dead cells were analyzed. E. The relationship between the local strain and percent dead cells was analyzed using the previously found local strain and dead cells information.

static culture (Fig. 1 A).

2.2. Micromechanical environment analysis

The local mechanical responses of each construct were measured using a previously established protocol (Buckley et al., 2010, 2008). Each construct was bisected into hemi-cylinders. Of the two hemi-cylinders, one was stained with 14 μg/mL 5-dichlorotriazinyl-amino-fluorescein (Molecular Probes, Grand Island, NY) for 30 min, and the other was kept in phosphate-buffered saline (PBS, Corning Cellgro, Manassas, VA) throughout the experiment as a control. Stained constructs were washed in PBS for 20 min and mounted between two parallel plates of a tissue deformation imaging stage (TDIS). Constructs were mounted in two orientations to study both the isotropic plane (n = 6, 3 with honeycomb and 3 with sponge) and the orthotropic plane (n = 8, 3 with honeycomb and 5 with sponge) (Fig. 1 B).

The TDIS was placed on an inverted Zeiss LSM 510 5 live confocal microscope with a Zeiss 5 × objective (Carl Zeiss AG, Oberkochen, Germany). A triangle displacement function with an amplitude of 750 μm was applied at 0.1 mm/s. The compression video was recorded at a frame rate of 20 frames per second. The local Lagrange strain was obtained by analyzing compression videos using NCORR, an open-source Digital Image Correlation (DIC) program (Blaber et al., 2015). Local deformation from the compression videos was tracked with subset spacing of 31.2 μm and a subset radius of 62.4 μm. All three local strain components (ε_{xx}, ε_{xy}, and ε_{yy}) were extracted and linearly interpolated to match the percent cell death grid. The strain norm of each subset was obtained by calculating the Euclidean norm of all strain tensors.

2.3. Cell death analysis

Chondrocyte death was imaged by adding 2 μM ethidium homodimer − 1 (Invitrogen, Waltham, MA) 3 h following the compression. The time frame was chosen based on a previous finding that nearly all cell death occurred within 3 h post physical stimuli (Bartell et al., 2015). Compressed constructs were stained for 30 min. Subsequently, the compressed region of each construct was imaged in a z-stack spaced at 15 μm with a total height of 150 μm. The z-stack images of each construct were projected into a single image. Each paired control sample was stained with 2 μM ethidium homodimer – 1 and calcein AM (Invitrogen, Waltham, MA) for 30 min at the end of the experiment. The control samples were subsequently imaged in the same fashion as the compressed constructs.

Images were processed using a watershed-based algorithm (Bartell et al., 2017) to identify dead cells and collagen scaffolds. Live and dead cells of the control samples were identified using the same analysis method. The number of dead cells within the compressed samples was summed within 140 μm by 140 μm grids. The total number of cells within each grid was calculated using the control sample, and the total number of cells in each grid was adjusted based on the presence of collagen scaffolds (Fig. 1 C).

2.4. Local deformation modes analysis

From the recorded compression videos, local deformation modes were identified as the classic regions of scaffold deformation (elastic, buckled, and densified regions) derived from the stress–strain curves and the visual cues (Kim et al., 2022; Middendorf et al., 2017b). These correlate to the elastic, plateau, and densified regions of the stress–strain plot of a porous solid under compression (Gibson, 2005). A gaussian summation model was fitted to the strain norm distribution of each collagen scaffold type from 5%, to 30% applied bulk strain with a 5% interval (Appendix A, B, C and D). Three gaussian distributions were fitted, and the mean and standard deviation of each distribution were obtained. If the mean was below 0.1 strain norm, the distribution was defined as elastic, while if the mean was between 0.1 and 0.25, the distribution was considered as buckled. The mean strain norm above 0.25 was considered as densified. Means and standard distributions were obtained from the summation models. Means of each category were averaged, and root sum squares were calculated. In addition, the percentage of each deformation mode was analyzed by calculating the area under each gaussian distribution.

2.5. Statistical analysis

A two-way analysis of variance was used to find the statistical significance of strain and cell death among elastic, buckled, and densified regions within each type of collagen scaffold. A one-way analysis of variance was used to find statistical significance in cell death among deformation modes as well as cell viability in control samples. A two-sample Kolmogorov-Smirnov test was used to find the statistical significance among the bulk-strain dependent strain distributions. p-values<0.05 were considered statistically significant.

3. Results

3.1. Failure patterns and local instabilities in the isotropic and the orthotropic planes

The isotropic (Video 1 and 2) and orthotropic planes of tissue-engineered constructs displayed distinct mechanical responses (Video 3 and 4). In the isotropic plane, the first layer of pores located closer to the boundary deformed, and subsequent layers of pores collapsed. During the compression, these pores displayed large lateral deformation, and the scaffold walls were buckled (white arrows, Fig. 2A). The local axial strain was concentrated where the scaffold walls were buckled or densified (red region, Fig. 2B). Axial strain ranged from −0.1 to −0.25 for buckled walls, and densified walls had strain lower than −0.25, reaching almost −0.5. Cell death was observed in regions with high deformation (Fig. 2C). In the orthotropic plane, local buckling initiated at individual sites on scaffold walls and propagated across the construct to form a global collapse band (white arrow, Fig. 2D). Like the isotropic plane, both the local buckling and the global collapse band were reflected in the local strain distribution (Fig. 2E). The global collapse band was characterized by an axial strain of −0.5, and the local strain gradient was formed around the collapse band. Cell death was observed in regions where the deformation was high (Fig. 2F).

3.2. Local deformation modes and cell death analysis

The large strain gradients observed at 30% bulk strain were also seen at lower bulk strain levels. We looked at the deformation and strain patterns at 15% bulk strain to clearly understand the spatial distribution of the strains. At 15% bulk strain, both planes had mostly elastically deformed pores, and a small population of buckled and densified pores (Fig. 3). Such different levels of pore deformation (Fig. 3A and D) corresponded to different levels of local strain. The densified region had a local compressive strain higher than 0.25, the buckled region contained local strains ranging from 0.10 to 0.25, while the elastic region had a strain below 0.10 (Fig. 3B and E). The strain distribution patterns were clearly multimodal with three distinct deformation modes at different strain levels. These three distinct deformation modes were apparent in the local strain histograms (Fig. 3C and F) and well modeled by a function composed of the sum of three gaussians. In the isotropic plane, the gaussian distribution that represented the elastic mode had a strain of 0.07 ± 0.03, the buckled mode had 0.22 ± 0.06, and the densified mode had 0.34 ± 0.05. In the orthotropic plane, the gaussian distribution that represented the elastic mode had a strain of 0.05 ± 0.02, the buckled mode had 0.11 ± 0.04, and the densified region had 0.28 ± 0.05.

We observed scaffolds at various applied bulk strain levels during loading (Fig. 4). The local strain distribution at each applied bulk strain

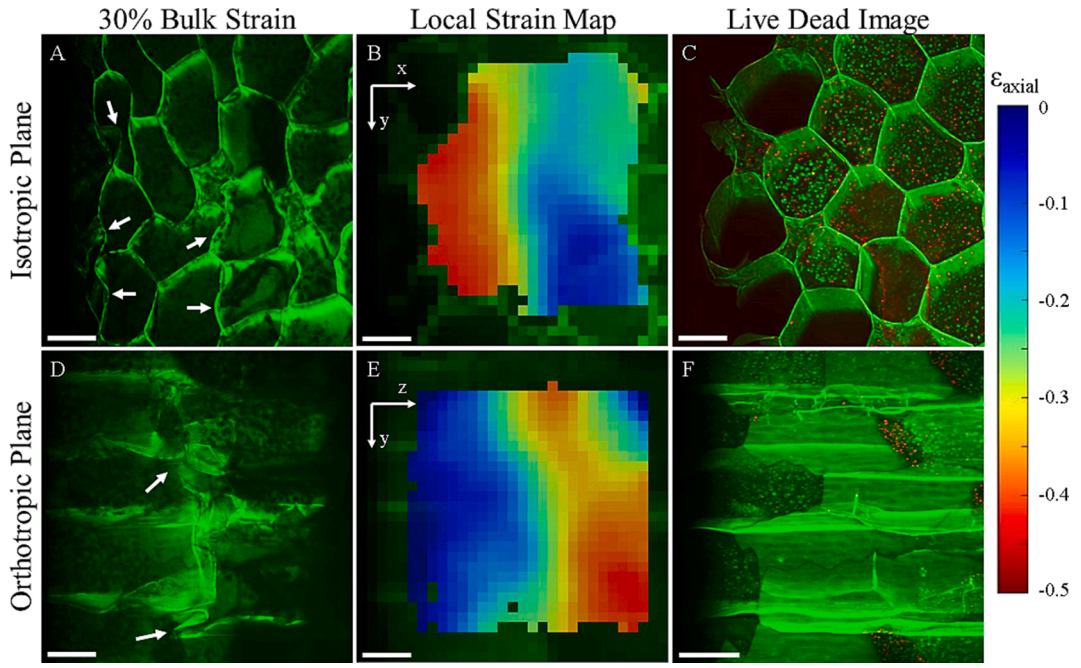

Fig. 2. Mechanical behavior of the isotropic and orthotropic planes. A. Buckled scaffold walls were detected at 30% bulk strain in the isotropic plane. B. Buckled scaffold walls were manifested as high compressive local strain. C. Dead cells were imaged three hours after the compression. D. In the orthotropic plane, global collapse band was detected at 30% bulk strain. E. Global collapse band was detected as high compressive local strain. F. Dead cells were detected in regions that developed global collapse band.

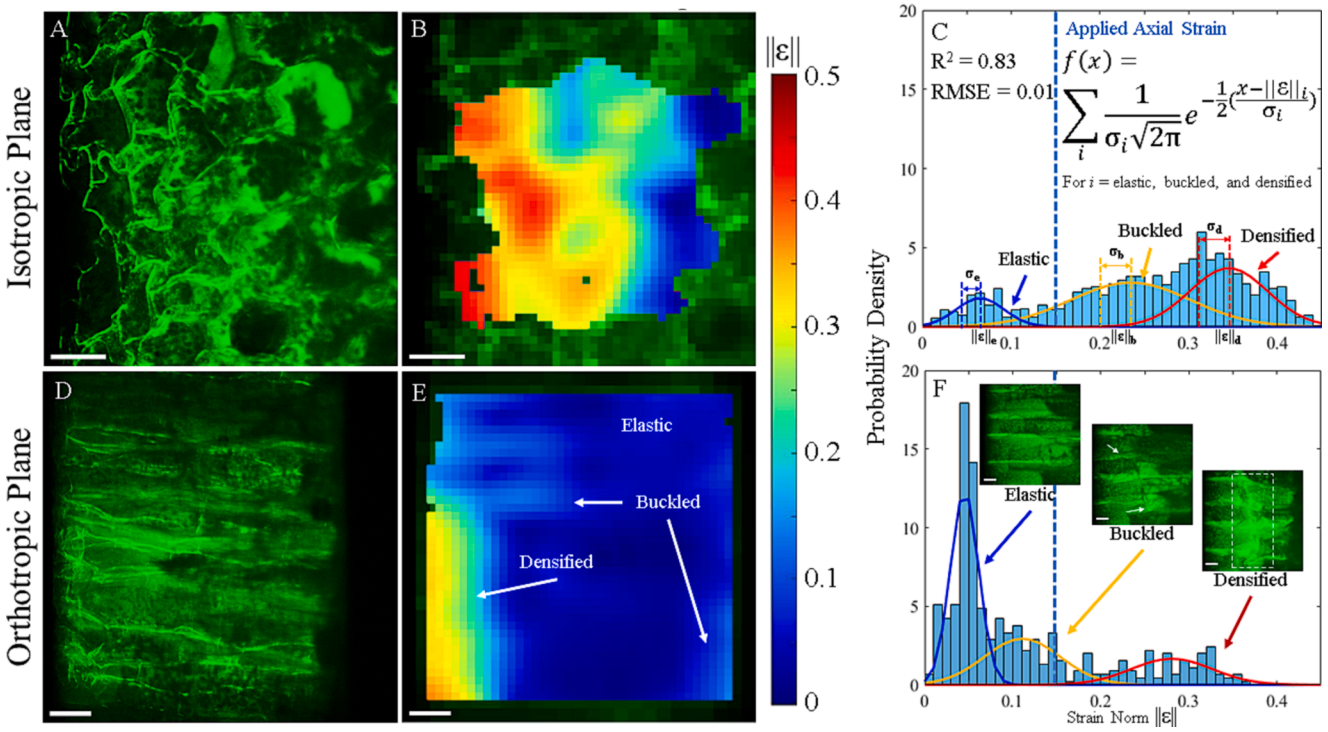

Fig. 3. Deformation mode analysis utilizing strain norm distribution and gaussian mixture model. A. Compressive deformation of sponge scaffold in the isotropic plane under 15% bulk strain. B. Local compressive strain map of the deformed plane. We see elastic mode from 0 to −0.1, buckled mode from −0.1 to −0.25, and densified mode had local compressive below −0.25. C. Gaussian mixture model was fitted to identify elastic, buckled, and densified mode. D. Compressive deformation of sponge scaffold in the orthotropic plane under 15% bulk strain. E. Local compressive strain map showing elastic, buckled, and densified modes. F. Gaussian mixture model identifying each deformation mode with representative deformation images.

(5, 15, and 30%) was distinct from one another ($p < 0.01$). However, there was no difference in the strain distributions between the two types of scaffolds at each applied bulk strain ($p > 0.6$). In general, at lower bulk strain levels, over 80% of the scaffolds experienced elastic deformation (Fig. 4, B, D, and E), except for honeycomb scaffolds in the isotropic plane (Fig. 4A). Interestingly, >50% of the isotropic plane of

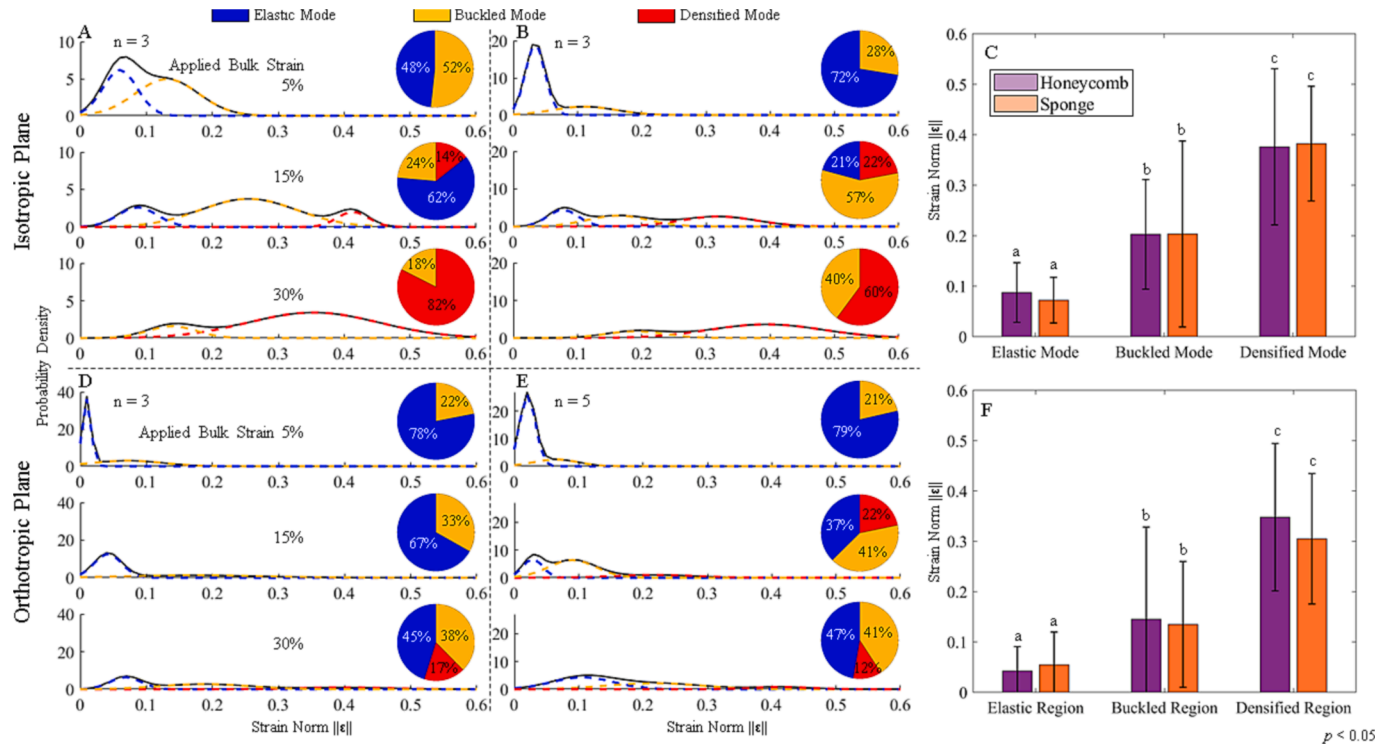

Fig. 4. Strain distribution and gaussian mixture analysis. A. Strain distribution of honeycomb scaffolds in the isotropic plane as applied bulk strain increased from 5% to 30%. B. Strain distribution of sponge scaffolds in the isotropic plane. C. Average strain norm of each deformation mode gradually increased from elastic to densified mode in the isotropic plane. There was no difference between the two types of scaffolds at each mode. D. Strain distribution of honeycomb scaffolds in the orthotropic plane as applied bulk strain increased from 5% to 30%. E. Strain distribution of sponge scaffolds in the orthotropic plane. F. Average strain norm at each mode in the orthotropic plane.

the honeycomb scaffolds experienced the buckled deformation mode at 5% applied bulk strain. As the bulk strain level increased, the percentage of regions that experienced buckled and densified deformation increased. On the other hand, the orthotropic plane had only 10–15% densified region at 30% applied bulk strain, which is much smaller compared to the isotropic plane (60–80% densified region). Averaged

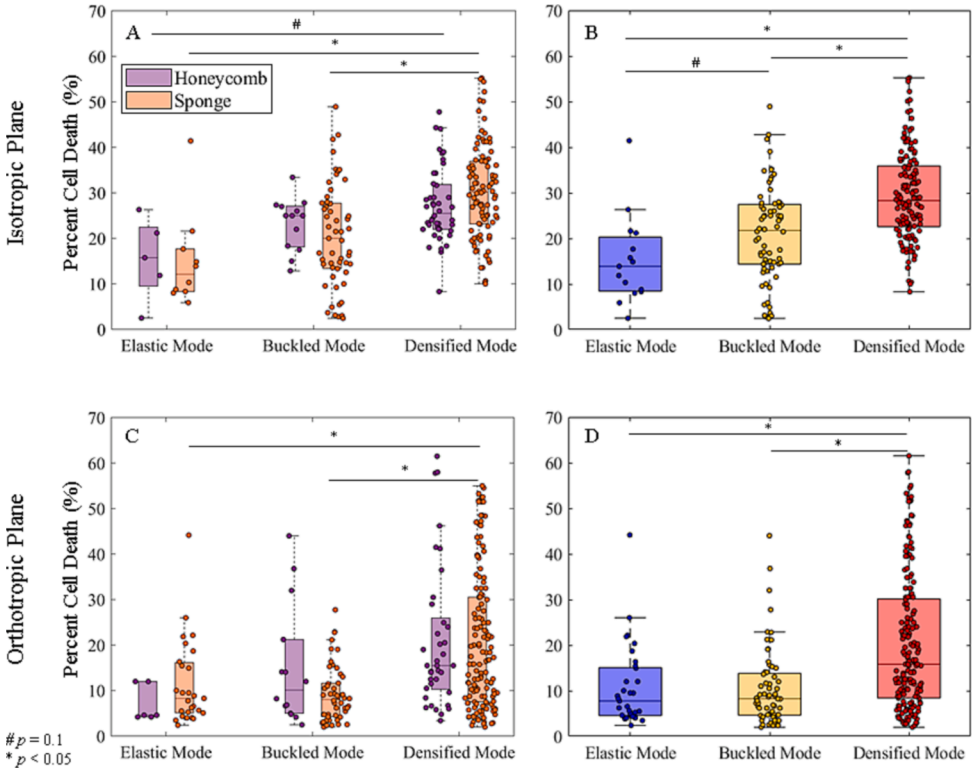

Fig. 5. Deformation mode and percent cell death. A. Percent cell death in honeycomb and sponge scaffolds at each mode in the isotropic plane. There was no difference in cell death between the two types of scaffolds at each mode. Sponge scaffold had an increase in percent cell death at densified mode. B. Combined percent cell death data showed that there was an increasing trend from elastic to buckled mode, and increased percent cell death from buckled to densified mode. C. There was no difference in percent cell death between elastic mode and buckled mode in both types of collagen scaffold in the orthotropic plane. There was an increase in percent cell death from buckled mode to densified mode in sponge scaffolds. D. Percent cell death was increased in densified mode compared to both elastic and buckled mode.

strain norm level revealed that in both planes (Fig. 4C and F, Appendix A and B), there was no difference in the strain norm level at each deformation mode between the two types of collagen scaffolds ($p > 0.99$). The strain norm increased as the construct deformation moved from the elastic to densified mode ($p < 0.015$). More interestingly, strain norm levels in all modes were lower in the orthotropic plane than the isotropic plane. Overall, the isotropic plane had both a larger percentage of buckled and densified regions and a higher strain norm level at each deformation mode compared to the orthotropic plane.

To understand the relationship between scaffold deformation mode and cell viability, we compared percent cell death data for each type of scaffold in the elastic, buckled, and densified mode. At 30% applied bulk strain, the percent cell death within these regions (Fig. 5) was extracted and plotted. Cell death in both the isotropic (Fig. 5A) and orthotropic (Fig. 5C) planes showed that there was no difference in cell death distribution within each deformation mode between the honeycomb and sponge scaffolds ($p > 0.5$). In the isotropic plane (Fig. 5A), there was no difference in cell death between the elastic and the buckled mode for both honeycomb and sponge scaffolds ($p > 0.6$). For the densified mode, cell death in the honeycomb scaffolds showed an increasing trend compared to the elastic mode ($p = 0.12$), but had no difference compared to the buckled mode ($p = 0.79$). For sponge scaffolds, cell death was higher in the densified mode than the elastic ($p < 0.001$) and the buckled ($p < 0.001$) modes. In the orthotropic plane (Fig. 5C), cell death in honeycomb scaffolds had no difference among the deformation modes ($p > 0.16$). Cell death in the densified mode of the sponge scaffold was increased from the elastic ($p < 0.05$) and buckled ($p < 0.001$) mode, but there was no difference between the elastic and buckled modes ($p = 0.98$). Collectively, these data show that the scaffold orientation is far more important than the scaffold architecture for chondrocyte viability.

To analyze the relationship more clearly between cell death and deformation mode, we combined the data for each scaffold architecture. Combined cell death data in the isotropic plane (Fig. 5B) showed that there was an increasing trend in cell death ($p = 0.10$) from the elastic to the buckled region, and increased cell death in the densified region compared to the elastic ($p < 0.001$) and buckled ($p < 0.001$) regions. In the orthotropic plane (Fig. 5D), there was no difference in cell death between the elastic and buckled modes ($p = 1$). Cell death was higher in the densified mode compared to the elastic ($p < 0.001$) and buckled ($p < 0.001$) modes.

4. Discussion

This study identified the relationship between the chondrocyte viability and their micromechanical environment in tissue-engineered constructs during quasi-static loading. More specifically, we investigated how scaffold architecture influences local strain distribution and subsequent cell death. We utilized fast confocal microscopy and DIC to understand how deformation modes in porous collagen scaffolds under load control cell viability. Our data showed that the local instabilities are directly linked to cell death. We identified three deformation modes in tissue-engineered cartilage constructs, elastic, buckled, and densified. The overall strain distribution of the constructs was well described by a summation of gaussian distributions representing each of the modes. Notably, cell viability was directly linked to these deformation modes, and there was no difference in cell death between the two types of scaffolds. Overall, these results showed that (i) under load, porous collagen scaffolds experienced three distinct modes generated by local instabilities, (ii) local instabilities are the primary mechanical driver for cell death, and (iii) the orientation of the scaffold is more important for cell viability than the type of scaffold.

We observed compression-induced instabilities in both planes (Fig. 2). Each plane had a distinct deformation pattern due to the differences in the effective length of structures experiencing buckling. In the isotropic plane, the effective length of the material was approximately the diameter of each pore which ranged from 200 to 300 μm. This short effective length combined with the pore architecture created a relatively uniform strain gradient within the construct (Fig. 3 B) along with the higher lateral strains compared to that of orthotropic plane (Appendix F). The orthotropic plane's effective length was longer at roughly 1.5 mm, which corresponds to the height of the scaffold. Under compression, the constructs developed local instabilities that propagated into a global collapse band, which was not observed in the isotropic plane. The local and global instabilities in the orthotropic plane resulted in regions with highly concentrated strain>0.25 compressive strain (Fig. 3E).

These distinct mechanical behaviors between the two planes were well characterized by the gaussian summation models of strain norm distributions (Appendix A, B, C and D, $R^2 > 0.53$, RMSE < 0.15). At 30% applied bulk strain, almost all regions in the isotropic plane experienced buckled or densified deformation, indicating a relatively uniform strain gradient within the construct. In the orthotropic plane, almost 40% of the construct experienced elastic deformation, suggesting a concentrated deformation around the global collapse band (Video 3 and 4). Notably, there was no difference in strain level per deformation mode between the two types of collagen scaffolds (Fig. 4 C and F), though each type of collagen scaffold had distinct strain distributions in both planes (Appendix I, $p < 0.01$). This orientation-dependent strain distribution created different micromechanical environments for chondrocytes seeded on collagen scaffolds, which greatly influenced the cell viability. Overall, these results indicate that the macro-architecture, such as the orientation, has a greater influence on the deformation modes scaffolds exhibit under load than the micro-architectural features, such as the presence of smaller pores (50 ~ 150 um) in sponge scaffolds.

The identified deformation modes in both planes significantly impacted cell death (Fig. 5). In both planes, the level of cell death in regions that exhibited the elastic deformation mode was not different from the controlled samples (Appendix J, $p > 0.26$). Notably, cell death increased from the elastic to the densified mode (Fig. 5 B and D), but there was no difference in cell death between the elastic and buckled modes or between the two types of scaffolds for any of the modes (Fig. 5 A and C). This suggests that the threshold for cell death is the densified deformation mode for tissue-engineered cartilage constructs, which implies that preventing densification in porous scaffolds is crucial for preventing cell death. Collectively, our data show that having an orthotropic plane within the collagen scaffolds and aligning the plane with the direction of *in vivo* load might be crucial for preventing cell death in tissue-engineered cartilage constructs after implantation.

Our results show that chondrocytes grown on porous collagen scaffolds under quasi-static compression have a similar threshold for chondrocyte death observed in native tissues under high-speed impact loading which was around 0.1 strain norm (Bartell et al., 2015). However, the level of cell death was lower in tissue-engineered constructs compared to native cartilage tissue. In the buckled mode, the average strain norm level was approximately 0.2 for both planes, which resulted in 10% to 20% cell death. In native cartilage tissue, 0.2 strain norm resulted in almost 70% cell death. In addition, the average strain norm level was 0.4 for the densified mode which resulted in 20% to 30% cell death. In native tissue, this level of strain norm should have resulted in 100% cell death. The discrepancy most likely originated from the loading rate and architectural features of collagen scaffolds. High speed impact loading created a large hydrostatic pressure within native tissue which was absent in the tissue-engineered construct. In addition, chondrocytes in native tissue experienced extracellular matrix to cell compression while chondrocytes in tissue-engineered constructs mostly experienced collagen scaffold walls to cell compression. Furthermore, instabilities in collagen scaffolds created regions of high strain rates that may be harmful for cells. This discrepancy further highlights the unique micromechanical environment of tissue-engineered constructs that was heavily influenced by the architectural features of collagen scaffolds.

The limitations of this study arise from differences between *in vivo* and *in vitro* boundary conditions. While constructs in this study were

loaded in unconfined compression, constructs implanted into focal defects *in vivo* can experience a variety of boundary conditions ranging from confined compression to unconfined compression. Confined compression will result in a higher hydrostatic pressure compared to the unconfined compression boundary condition which can impact cell death. In this study, we utilized a quasi-static loading condition to allow fluid to escape the sample, hence decoupling the effect of construct deformation on chondrocyte viability from the potential influence of hydrostatic pressure. Additionally, three-dimensional deformation of the constructs was observed during compression (Video 3 and 4). Our strain mapping technique, a two-dimensional analysis, cannot capture all three-dimensional strain components, which might explain the substantial variability in cell viability. In addition, the technique often loses up to 8% of the total data set on the local regions with extreme three-dimensional deformation. These regions were removed from strain-cell death correlation analysis. Lastly, we did not measure the forces during the experiments or the mechanical properties of the constructs. However, the mechanical properties and the stress–strain behaviors of the constructs were analyzed in previous studies (Kim et al., 2022; Middendorf et al., 2017a).

Previous studies in cellular solids and foams primarily focused on identifying deformation modes from the macro stress–strain curves (Andrews et al., 1999; Gaitanaros et al., 2012; Gong et al., 2005; Jang and Kyriakides, 2009). Such approaches have been adopted to study the mechanical response of collagen scaffolds (Gibson, 2005; Harley et al., 2007). However, recent findings suggest that analyzing only the stress–strain curves may not be sufficient to fully characterize the mechanical responses of cellular solids and foams (Aakash et al., 2019; Kim et al., 2022). Furthermore, the mechanical consequences from the architectural features of collagen scaffolds and their effects on cell viability were not previously well characterized. This study provides insight on the relationship between the architectural features of collagen scaffolds and the local micromechanical response and the influence of this micromechanical environment on chondrocyte viability. Overall, our data suggest that minimizing buckling and densification in collagen scaffolds, by reinforcing the pores with more fibers or filling in the pores with stiffer hydrogel, is crucial for minimizing cell death in tissue-engineered cartilage constructs.

CRediT authorship contribution statement

Byumsu Kim: Validation, Methodology, Investigation, Formal analysis, Data curation, Conceptualization, Project administration, Writing - original draft, Writing - review & editing. **Nikolaos Bouklas:** Supervision, Methodology, Conceptualization, Visualization, Writing - review & editing. **Itai Cohen:** Supervision, Methodology, Investigation, Conceptualization, Writing - review & editing. **Lawrence J. Bonassar:** Visualization, Validation, Supervision, Resources, Project administration, Methodology, Investigation, Conceptualization, Writing - review & editing.

Declaration of Competing Interest

The authors declare that they have no known competing financial interests or personal relationships that could have appeared to influence the work reported in this paper.

Acknowledgments

This work made use of the Cornell Center for Materials Research Shared Facilities which are supported through the NSF MRSEC program (DMR-1719875). This study was partially funded by NSF CMMI 2129776, NSF CMMI 1927197, and NSF DMR 1807602. The authors thank Dr. Stavros Gaitanaros and Dr. Jill Middendorf for helpful discussion.

Appendix A. Supplementary data

Supplementary data to this article can be found online at https://doi.org/10.1016/j.jbiomech.2023.111591.

References

Aakash, B.S., Bi, S., Shields, M.D., Gaitanaros, S., 2019. On the high-temperature crushing of metal foams. Int. J. Solids Struct. 174–175, 18–27. https://doi.org/10.1016/j.ijsolstr.2019.06.007.

Anderson, D.E., Williams, R.J., DeBerardino, T.M., Taylor, D.C., Ma, C.B., Kane, M.S., Crawford, D.C., 2017. Magnetic Resonance Imaging Characterization and Clinical Outcomes After NeoCart Surgical Therapy as a Primary Reparative Treatment for Knee Cartilage Injuries. Am. J. Sports Med. 45, 875–883. https://doi.org/10.1177/0363546516677255.

Andrews, E., Sanders, W., Gibson, L.J., 1999. Compressive and tensile behaviour of aluminum foams. Mater. Sci. Eng. A 270, 113–124. https://doi.org/10.1016/S0921-5093(99)00170-7.

Bartell, L.R., Bonassar, L.J., Cohen, I., 2017. A watershed-based algorithm to segment and classify cells in fluorescence microscopy images (No. arXiv:1706.00815). arXiv. https://doi.org/10.48550/arXiv.1706.00815.

Bartell, L.R., Fortier, L.A., Bonassar, L.J., Cohen, I., 2015. Measuring microscale strain fields in articular cartilage during rapid impact reveals thresholds for chondrocyte death and a protective role for the superficial layer. J. Biomech. 48, 3440–3446. https://doi.org/10.1016/j.jbiomech.2015.05.035.

Blaber, J., Adair, B., Antoniou, A., 2015. Ncorr: Open-Source 2D Digital Image Correlation Matlab Software. Exp. Mech. 55, 1105–1122. https://doi.org/10.1007/s11340-015-0009-1.

Bonnevie, E.D., Delco, M.L., Bartell, L.R., Jasty, N., Cohen, I., Fortier, L.A., Bonassar, L.J., 2018. Microscale frictional strains determine chondrocyte fate in loaded cartilage. J. Biomech. 74, 72–78. https://doi.org/10.1016/j.jbiomech.2018.04.020.

Bowles, R.D., Williams, R.M., Zipfel, W.R., Bonassar, L.J., 2010. Self-Assembly of Aligned Tissue-Engineered Annulus Fibrosus and Intervertebral Disc Composite Via Collagen Gel Contraction. Tissue Eng. A 16, 1339–1348. https://doi.org/10.1089/ten.tea.2009.0442.

Brittberg, M., Recker, D., Ilgenfritz, J., Saris, D.B.F., 2018. Matrix-Applied Characterized Autologous Cultured Chondrocytes Versus Microfracture: Five-Year Follow-up of a Prospective Randomized Trial. Am. J. Sports Med. 46, 1343–1351. https://doi.org/10.1177/0363546518756976.

Buckley, M.R., Gleghorn, J.P., Bonassar, L.J., Cohen, I., 2008. Mapping the depth dependence of shear properties in articular cartilage. J. Biomech. 41, 2430–2437. https://doi.org/10.1016/j.jbiomech.2008.05.021.

Buckley, M.R., Bergou, A.J., Fouchard, J., Bonassar, L.J., Cohen, I., 2010. High-resolution spatial mapping of shear properties in cartilage. J. Biomech. 43, 796–800. https://doi.org/10.1016/j.jbiomech.2009.10.012.

Buschmann, M.D., Gluzband, Y.A., Grodzinsky, A.J., Kimura, J.H., Hunziker, E.B., 1992. Chondrocytes in agarose culture synthesize a mechanically functional extracellular matrix. J. Orthop. Res. 10, 745–758. https://doi.org/10.1002/jor.1100100602.

Buschmann, M.D., Gluzband, Y.A., Grodzinsky, A.J., Hunziker, E.B., 1995. Mechanical compression modulates matrix biosynthesis in chondrocyte/agarose culture. J. Cell Sci. 108, 1497–1508. https://doi.org/10.1242/jcs.108.4.1497.

Crawford, D.C., DeBerardino, T.M., Williams, R.J., 2012. NeoCart, an autologous cartilage tissue implant, compared with microfracture for treatment of distal femoral cartilage lesions: An FDA phase-II prospective, randomized clinical trial after two years. J. Bone Joint Surg. Ser. A 94, 979–989. https://doi.org/10.2106/JBJS.K.00533.

Cross, V.L., Zheng, Y., Won Choi, N., Verbridge, S.S., Sutermaster, B.A., Bonassar, L.J., Fischbach, C., Stroock, A.D., 2010. Dense type I collagen matrices that support cellular remodeling and microfabrication for studies of tumor angiogenesis and vasculogenesis in vitro. Biomaterials 31, 8596–8607. https://doi.org/10.1016/j.biomaterials.2010.07.072.

Delco, M.L., Bonnevie, E.D., Bonassar, L.J., Fortier, L.A., 2018. Mitochondrial dysfunction is an acute response of articular chondrocytes to mechanical injury. J. Orthop. Res. 36, 739–750. https://doi.org/10.1002/jor.23651.

Gaitanaros, S., Kyriakides, S., Kraynik, A.M., 2012. On the crushing response of random open-cell foams. Int. J. Solids Struct. 2733–2743. https://doi.org/10.1016/j.ijsolstr.2012.03.003.

Genes, N.G., Rowley, J.A., Mooney, D.J., Bonassar, L.J., 2004. Effect of substrate mechanics on chondrocyte adhesion to modified alginate surfaces. Arch. Biochem. Biophys. 422, 161–167. https://doi.org/10.1016/j.abb.2003.11.023.

Gibson, L.J., 2005. Biomechanics of cellular solids. J. Biomech. 38, 377–399. https://doi.org/10.1016/j.jbiomech.2004.09.027.

Gong, L., Kyriakides, S., Jang, W.Y., 2005. Compressive response of open-cell foams. Part I: Morphology and elastic properties. Int. J. Solids Struct. 42, 1355–1379. https://doi.org/10.1016/j.ijsolstr.2004.07.023.

Guilak, F., 2000. The deformation behavior and viscoelastic properties of chondrocytes in articular cartilage. Biorheology 37, 27–44.

Guilak, F., Meyer, B., Ratcliffe, A., Mow, V., 1994. The effects of matrix compression on proteoglycan metabolism in articular cartilage explants. Osteoarthr. Cartil. 2, 91–101. https://doi.org/10.1016/S1063-4584(05)80059-7.

Guilak, F., Ratcliffe, A., Mow, V.C., 1995. Chondrocyte deformation and local tissue strain in articular cartilage: A confocal microscopy study. J. Orthop. Res. 13, 410–421. https://doi.org/10.1002/jor.1100130315.

Harley, B.A., Leung, J.H., Silva, E.C.C.M., Gibson, L.J., 2007. Mechanical characterization of collagen-glycosaminoglycan scaffolds. Acta Biomater. 3, 463–474. https://doi.org/10.1016/j.actbio.2006.12.009.

Jang, W.Y., Kyriakides, S., 2009. On the crushing of aluminum open-cell foams: Part I. Experiments. Int. J. Solids Struct. 46, 617–634. https://doi.org/10.1016/j.ijsolstr.2008.09.008.

Jiang, S., Guo, W., Tian, G., Luo, X., Peng, L., Liu, S., Sui, X., Guo, Q., Li, X., 2020. Clinical Application Status of Articular Cartilage Regeneration Techniques: Tissue-Engineered Cartilage Brings New Hope. Stem Cells Int. 2020, 5690252. https://doi.org/10.1155/2020/5690252.

Kim, B., Middendorf, J.M., Diamantides, N., Dugopolski, C., Kennedy, S., Blahut, E., Cohen, I., Bouklas, N., Bonassar, L.J., 2022. The Role of Buckling Instabilities in the Global and Local Mechanical Response in Porous Collagen Scaffolds. Exp. Mech. https://doi.org/10.1007/s11340-022-00853-7.

Kreuz, P.C., Müller, S., Freymann, U., Erggelet, C., Niemeyer, P., Kaps, C., Hirschmüller, A., 2011. Repair of Focal Cartilage Defects with Scaffold-Assisted Autologous Chondrocyte Grafts: Clinical and Biomechanical Results 48 Months After Transplantation. Am. J. Sports Med. 39, 1697–1706. https://doi.org/10.1177/0363546511403279.

Lee, C.S.D., Gleghorn, J.P., Won Choi, N., Cabodi, M., Stroock, A.D., Bonassar, L.J., 2007. Integration of layered chondrocyte-seeded alginate hydrogel scaffolds. Biomaterials 28, 2987–2993. https://doi.org/10.1016/j.biomaterials.2007.02.035.

Lee, H., Gu, L., Mooney, D.J., Levenston, M.E., Chaudhuri, O., 2017. Mechanical confinement regulates cartilage matrix formation by chondrocytes. Nat. Mater 16, 1243–1251. https://doi.org/10.1038/nmat4993.

Madden, R.M.J., Han, S.-K., Herzog, W., 2015. The effect of compressive loading magnitude on in situ chondrocyte calcium signaling. Biomech. Model. Mechanobiol. 14, 135–142. https://doi.org/10.1007/s10237-014-0594-4.

Middendorf, J.M., Griffin, D.J., Shortkroff, S., Dugopolski, C., Kennedy, S., Siemiatkoski, J., Cohen, I., Bonassar, L.J., 2017a. Mechanical properties and structure-function relationships of human chondrocyte-seeded cartilage constructs after in vitro culture. https://doi.org/10.1002/jor.23535.

Middendorf, J.M., Shortkroff, S., Dugopolski, C., Kennedy, S., Siemiatkoski, J., Bartell, L. R., Cohen, I., Bonassar, L.J., 2017. In vitro culture increases mechanical stability of human tissue engineered cartilage constructs by prevention of microscale scaffold buckling. Journal of Biomechanics 64, 77–84. https://doi.org/10.1016/j.jbiomech.2017.09.007. ISSN 0021–9290.

Middendorf, J.M., Diamantides, N., Shortkroff, S., Dugopolski, C., Kennedy, S., Cohen, I., Bonassar, L.J., 2020a. Multiscale Mechanics of Tissue Engineered Cartilage Grown from Human Chondrocytes and Human Induced Pluripotent Stem Cells. J. Orthop Res. jor.24643. https://doi.org/10.1002/jor.24643.

Middendorf, J.M., Dugopolski, C., Kennedy, S., Blahut, E., Cohen, I., Bonassar, L.J., 2020b. Heterogeneous matrix deposition in human tissue engineered cartilage changes the local shear modulus and resistance to local construct buckling. J. Biomech. 105, 109760 https://doi.org/10.1016/j.jbiomech.2020.109760.

Moran, J.M., Pazzano, D., Bonassar, L.J., 2003. Characterization of Polylactic Acid-Polyglycolic Acid Composites for Cartilage Tissue Engineering. Tissue Eng. 9, 63–70. https://doi.org/10.1089/107632703762687546.

Murphy, C.M., Haugh, M.G., O'Brien, F.J., 2010. The effect of mean pore size on cell attachment, proliferation and migration in collagen–glycosaminoglycan scaffolds for bone tissue engineering. Biomaterials 31, 461–466. https://doi.org/10.1016/j.biomaterials.2009.09.063.

Murphy, C.M., O'Brien, F.J., 2010. Understanding the effect of mean pore size on cell activity in collagen-glycosaminoglycan scaffolds. Cell Adh. Migr. 4, 377–381. https://doi.org/10.4161/cam.4.3.11747.

Ossendorf, C., Kaps, C., Kreuz, P.C., Burmester, G.R., Sittinger, M., Erggelet, C., 2007. Treatment of posttraumatic and focal osteoarthritic cartilage defects of the knee with autologous polymer-based three-dimensional chondrocyte grafts: 2-year clinical results. Arthritis Res. Ther. 9, R41. https://doi.org/10.1186/ar2180.

Rouillard, A.D., Berglund, C.M., Lee, J.Y., Polacheck, W.J., Tsui, Y., Bonassar, L.J., Kirby, B.J., 2011. Methods for Photocrosslinking Alginate Hydrogel Scaffolds with High Cell Viability. Tissue Eng. Part C Methods 17, 173–179. https://doi.org/10.1089/ten.tec.2009.0582.

Schneider, U., Rackwitz, L., Andereya, S., Siebenlist, S., Fensky, F., Reichert, J., Löer, I., Barthel, T., Rudert, M., Nöth, U., 2011. A Prospective Multicenter Study on the Outcome of Type I Collagen Hydrogel-Based Autologous Chondrocyte Implantation (CaReS) for the Repair of Articular Cartilage Defects in the Knee. Am. J. Sports Med. 39, 2558–2565. https://doi.org/10.1177/0363546511423369.

Silver, F.H., Ebrahimi, A., Snowhill, P.B., 2002. Viscoelastic Properties of Self-Assembled Type I Collagen Fibers: Molecular Basis of Elastic and Viscous Behaviors. Connect. Tissue Res. 43, 569–580. https://doi.org/10.1080/03008200290001302.

Vansusante, J., Buma, P., Homminga, G., Vandenberg, W., Veth, R., 1998. Chondrocyte-seeded hydroxyapatite for repair of large articular cartilage defects. A pilot study in the goat. Biomaterials 19, 2367–2374. https://doi.org/10.1016/S0142-9612(98)00158-6.

Wang, J.L., Parnianpour, M., Shirazi-Adl, A., Engin, A.E., 1997. Failure criterion of collagen fiber: Viscoelastic behavior simulated by using load control data. Theor. Appl. Fract. Mech. 27, 1–12. https://doi.org/10.1016/S0167-8442(97)00002-5.

Zak, L., Albrecht, C., Wondrasch, B., Widhalm, H., Vekszler, G., Trattnig, S., Marlovits, S., Aldrian, S., 2014. Results 2 Years After Matrix-Associated Autologous Chondrocyte Transplantation Using the Novocart 3D Scaffold: An Analysis of Clinical and Radiological Data. Am. J. Sports Med. 42, 1618–1627. https://doi.org/10.1177/0363546514532337.